Nonradiative transition dynamics in alexandrite

S. K. Gayen, W. B. Wang, V. Petričević, and R. R. Alfano
Institute for Ultrafast Spectroscopy and Lasers, Physics Department and Electrical Engineering Department, The City College of New York, New York, New York 10031

(Received 4 June 1986; accepted for publication 25 June 1986)

The first direct picosecond time-resolved measurement of the nonradiative transition dynamics between the excited $^4T_2$ pump band and the metastable ^2E storage level of the trivalent chromium ion in alexandrite is reported. The nonradiative relaxation times of 17 ps for intra-$^4T_2$ vibrational transitions, and 27 ps for $^4T_2 \rightarrow {}^2E$ electronic transition are obtained. The thermal repopulation rate of the $^4T_2$ state from the metastable ^2E level is of the order $3.5 \times 10^9\ s^{-1}$.

The recent renewed interest in tunable solid-state lasers based on vibronic transitions in transition-metal-ion-doped insulators was prompted by successful wavelength-tunable room-temperature operation of alexandrite[1] and emerald[2,3] lasers. These developments have made it imperative to study and investigate the various loss mechanisms which may impede laser action in those crystals. A detailed and quantitative understanding of the loss mechanisms is crucial in the selection and formulation of design criteria of these crystals. One such major loss mechanism is nonradiative (NR) relaxation. Although the theory of NR processes has evolved over the years, there is a paucity of experimental investigation of these processes among the excited states of the lasing transition-metal ions in tunable solid-state laser crystals to test these theories.

Recently, we have undertaken a research program to investigate, by time-resolved picosecond spectroscopy, the NR transition dynamics between different levels involved in laser action in a variety of transition-metal-ion-doped crystals. The objectives are to better understand the physics behind tunable solid-state lasers, and to accumulate data which may provide a crucial test to the existing theories for NR transitions as applied to transition-metal ions in insulators. In this letter, we present the first picosecond excite-and-probe measurements of the NR transition dynamics between the $^4T_2$ lasing level and the metastable ^2E storage level in alexandrite.

Alexandrite (Cr^{3+}:$BeAl_2O_4$) is a prototype of intermediate-field Cr^{3+}-activated crystals characterized by broadband $^4T_2 \rightarrow {}^4A_2$ fluorescence. The homogeneously broadened, vibronic, four-level mode of laser action in alexandrite at room temperature is tunable over the 701–818 nm continuous range of this fluorescence band. In addition, alexandrite, like ruby, has been demonstrated to lase in a three-level mode, where the laser emission on the R line at 680.4 nm is due to the narrow-band $^2E \rightarrow {}^4A_2$ transition.[1]

The absorption spectrum of alexandrite is characterized by two broad bands attributed to the $^4A_2 \rightarrow {}^4T_2$ and $^4A_2 \rightarrow {}^4T_1$ transitions in Cr^{3+}. These broad bands serve as the optical pump bands, which relax rapidly and nonradiatively to the ^2E level. The $^2E \rightarrow {}^4T_2$ energy gap in alexandrite is only 800 cm^{-1}, which allows significant thermal repopulation of the $^4T_2$ state from the ^2E. The metastable ^2E state acts as a storage level for vibronic transitions from the $^4T_2$ state to the vibrational levels of the $^4A_2$ ground state.

Although the characteristics of the absorption, emission, excitation, and excited-state absorption (ESA) spectra as well as other spectroscopic properties of alexandrite are well documented,[1,4–7] to our knowledge no experimental measurement of nonradiative relaxation processes and transition dynamics among the excited states of Cr^{3+} ion in this crystal has yet been reported. Because of the relatively strong vibronic coupling of the $^4T_2$ state with the breathing modes and Jahn–Teller modes,[8] the $^4T_2 \rightarrow {}^2E$ transition is expected to be extremely fast.

In the present measurements, a 7-ps 527-nm pulse excites higher lying vibrational (HLV) states of the broad $^4T_2$ band. These excited vibrational states relax predominantly via NR transitions resulting in a growth of population in the zero and lower lying vibrational (LLV) states of $^4T_2$ and the metastable ^2E state. This growth of population is monitored by an infrared picosecond probe pulse which may be wavelength tuned from 2 to 5 μm. The kinetics of the excited-state transition is studied by measuring the change in optical absorption of the probe pulse as a function of pump-probe delay time. Details of the experimental arrangement, detection scheme, signal averaging, and processing technique have been reported elsewhere.[9]

The result of the present picosecond excite-and-probe measurement in alexandrite showing the time evolution of optical density (OD) at 3.4 μm is displayed in Fig. 1(a). The curve is characterized by a 20 ± 5 ps rise time (time for growth of OD from 10% to 90%) followed by a multicomponent decay. The faster component has a decay time (time for OD to fall from 90% to 10% of the peak value above the flat region) of $\sim 60 \pm 10$ ps, whereas the longer lifetime component does not exhibit any appreciable change within the time scale of this measurement.

To further understand this complicated behavior, we extend the present measurement to a probe wavelength of 2.4 μm, and the result is presented in Fig. 1(b). The salient features of the curve are a resolution-limited sharp rise followed by a 20 ± 5 ps decay. The key to the different behavior at the two probe wavelengths lies in the difference in energy of the photons used and the different transitions which may be initiated by those photons. With 3.4 μm as the probe wavelength, transitions from both ^2E to $^4T_2$ and zero-vibrational level to HLV levels of $^4T_2$ manifold are energetically possible. However, a 3.4-μm photon is not energetic enough to cause a transition even from any HLV state of $^4T_2$ to the

 0003-6951/86/340437-03$01.00

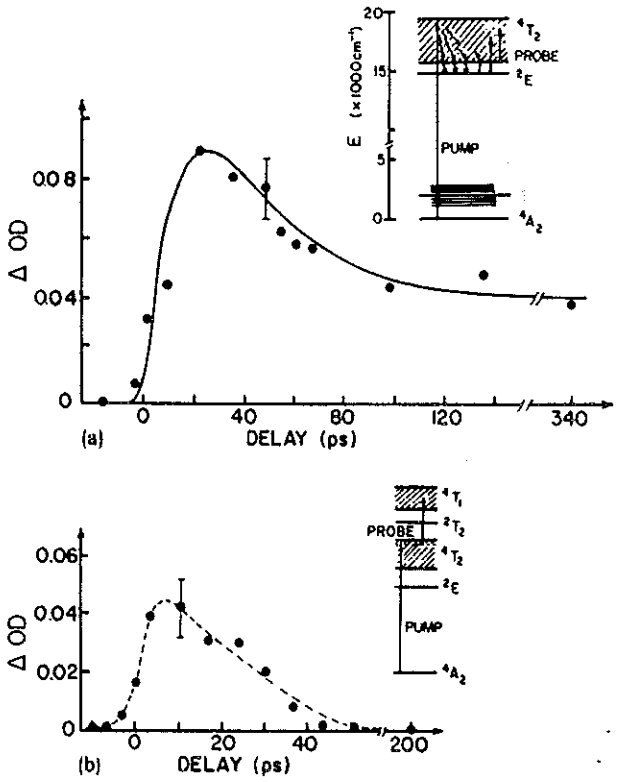

FIG. 1. Time evolution of the optical density (a) at 3.4 μm, and (b) at 2.4 μm in the ^2E and $^4T_2$ zero and lower lying vibrational states in alexandrite at room temperature. The sample is a rectangular parallelepiped 12 mm × 10 mm × 2.4 mm in dimension and contains 0.4 at. % of Cr^{3+}. Both the pump and probe pulses are linearly polarized parallel to the b axis of the alexandrite crystal, and traverse the sample almost collinearly (a crossing angle of 2°). The radii of the pump and the probe pulses at the sample positon are 0.6 mm and 0.5 mm, respectively. The absorption measurements were taken along the 2.4-mm path length of the sample. Insets show the relevant energy-level diagram of Cr^{3+}:$BeAl_2O_4$, and the pump, probe, and relaxation transitions. The zero time is accurate within 5 ps. Size of a typical error bar is shown. The solid curve in (a) is the computer fit to the experimental data represented by closed circles.

$^4T_1$ band. On the other hand, a 2.4-μm photon has sufficient energy to initiate transitions from ^2E to some HLV states of $^4T_2$, and from HLV states of $^4T_2$ to $^4T_1$ band. However, this energy is greater than the width of $^4T_2$ band, so the possibility of any transition from zero vibrational level of $^4T_2$ to HLV levels is ruled out.

We attribute the change in OD at 2.4 μm mainly to absorptive transition from HLV states of $^4T_2$ to the $^4T_1$ state. The contribution of $^2E \rightarrow {}^4T_2$ absorption is expected to be very small at this probe wavelength, because the energy of a 2.4-μm photon corresponds to a transition from ^2E to almost the high-energy end of the $^4T_2$ band and Franck–Condon overlap integrals for such transitions are vanishingly small. The resolution-limited rise time indicates the increase of population as long as the pump pulse is on. The 20 ± 5 ps decay time reflects the vibrational relaxation time of higher lying vibrational states of $^4T_2$ band which are excited by the pump pulse. This relaxation leads to growth of population in the zero vibrational level of the $^4T_2$ band and in the metastable ^2E level.

The change in OD at 3.4 μm is determined by the population of the two levels and the absorption cross sections for 3.4 μm photons from the two levels. So, the rise time of 20 ± 5 ps for the OD at 3.4 μm [Fig. 1(a)] is consistent with the 20 ± 5 ps vibrational relaxation time that populates the two levels. The flat region indicates that a quasithermal equilibrium has been reached between the ^2E and $^4T_2$ levels. Further depopulation of the excited states is expected to be predominantly due to radiative transitions. Since the room-temperature fluorescence lifetime of alexandrite is 262 μs, no appreciable change is observed in the time scale of this measurement. The 60 ± 10 ps lifetime component presumably reflects the nonequilibrium population kinetics among the ^2E and $^4T_2$ levels and is related to the "effective thermalization time."

A detailed and quantitative understanding of the experimental results may be obtained from a model study of the kinetics of excited-state population. The time evolution of the optical absorption from the excited ^2E and $^4T_2$ states following the excitation of some HLV states of the $^4T_2$ band is described by the excited-state absorption coefficient,

$$\alpha_e(t) = N_1(t)\sigma_1 + N_2(t)\sigma_2 , \qquad (1)$$

where N_1 and N_2 are instantaneous population densities (ions/cm^3) and σ_1 and σ_2 are cross sections for probe absorption in the ^2E and $^4T_2$ states, respectively. The transitions and rates are schematically shown in Fig. 2. The population kinetics of the $^4T_2$ and the ^2E states are governed by rate equations detailed elsewhere.[10]

Since the radiative lifetimes are of the order of milliseconds to microseconds, the radiative transition rates k_{10} and k_{20} are extremely small compared to nonradiative rates, and may be neglected in the kinetics study of the first few hundred picoseconds. The rate equations were solved numerically using the fourth-order Runge–Kutta method.[11] The pump pulse was approximated by a Gaussian of 7 ps FWHM. The fit to the experimental data using rates k, k_{12}, k_{21}, and σ's as variable parameters is displayed by the solid curve in Fig. 1(a). The arbitrary constants in the solution of the differential equations were determined from the initial condition that at $t = 0$ only the HLV states of $^4T_2$ band are populated; and the final condition that at sufficiently large times the population in the ^2E and $^4T_2$ states obeys the Boltzmann distribution law for thermal equilibrium population.[12] The values of the parameters obtained from the fit are $k = 6 \times 10^{10}$ s^{-1}, $k_{21} = 3.7 \times 10^{10}$ s^{-1}, $k_{12} = 3.5 \times 10^9$ s^{-1}, and $\sigma_2/\sigma_1 = 7.5$. It was observed that the fit is more sensitive

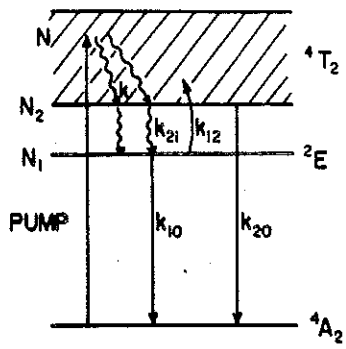

FIG. 2. Schematic diagram showing relevant transitions and transition rates. Here k is the intra-$^4T_2$ vibrational relaxation rate, k_{21} is $^4T_2 \rightarrow {}^2E$ electronic relaxation rate, k_{12} is thermal refilling rate of $^4T_2$ from ^2E, and k_{10} and k_{20} are radiative transition rates from ^2E and $^4T_2$ states, respectively.

to the sum $k_{12}+k_{21}$ than independently to k_{12} and k_{21}. The individual rates are estimated from thermal equilibrium Boltzmann condition.

The present picosecond excite-and-probe-absorption measurement together with the model fit yields a number of key relaxation times. The vibrational relaxation rate k is estimated to be $6\times10^{10}\ s^{-1}$, which implies a vibrational relaxation time of ~17 ps for transition from HLV states to the bottom of $^4T_2$ adiabatic potential energy parabola. This is consistent with 20 ± 5 ps obtained from experimental curves. The value of $3.7\times10^{10}\ s^{-1}$ for the nonradiative relaxation rate k_{21} for the electronic transition between the $^4T_2$ and ^2E levels leads to a relaxation time of ~27 ps. The thermal repopulation rate of the $^4T_2$ level from the ^2E storage level is obtained to be $3.5\times10^{9}\ s^{-1}$.

The intra-$^4T_2$ vibrational relaxation rate in alexandrite turns out to be comparable to $^4T_2\rightarrow{}^2E$ electronic nonradiative relaxation rate. This is unusual but not surprising, since a larger energy degradation ($\sim3400\ cm^{-1}$) is involved in vibrational relaxation than in electronic relaxation (800 cm^{-1}) for the 527-nm excitation of the $^4T_2$ band. This also implies that anharmonicities in the vibrations in the excited $^4T_2$ state of alexandrite are somewhat smaller, since vibrational relaxation is due to anharmonicities in the vibrations.[13]

The ratio of σ_2/σ_1 obtained from the fit was used with the experimentally measured value of α_e and experimental parameters such as pump-pulse energy, spot sizes of the pump and probe pulses, and Cr^{3+} ion density in the sample to estimate the absorption cross section at 3.4 μm from the excited states. The ESA cross section at 3.4 μm from the ^2E level is estimated to be $1.9\times10^{-18}\ cm^2$ and from $^4T_2$ state to be $1.4\times10^{-17}\ cm^2$. This factor-of-seven larger ESA cross section from the $^4T_2$ state as compared to that in ^2E state is consistent with the ESA measurements in the pump[5] and lasing[6,7] wavelength regions of alexandrite, where the initial level of ESA is designated to be the $^4T_2$ state. We believe even at the pump and lasing wavelengths ESA transitions initiate from ^2E level as well, but have a much smaller cross section than those from the $^4T_2$ state. However, the absolute magnitude of the infrared ESA cross section is significantly larger than the peak cross section ($\sim10^{-19}\ cm^2$) in the visible.

It is a pleasure to acknowledge the helpful discussions with Professor Ralph Bartram and Dr. Harold Samelson, and technical help from Professor Roger Dorsinville. The research is supported by Army Research Office and NASA.

[1]J. C. Walling, O. G. Peterson, H. P. Jenssen, R. C. Morris, and E. Wayne O'Dell, IEEE J. Quantum Electron. QE-16, 1302 (1980) and references therein.
[2]M. L. Shand and J. C. Walling, IEEE J. Quantum Electron. QE-18, 1829 (1982).
[3]J. Buchert, A. Katz, and R. R. Alfano, IEEE J. Quantum Electron. QE-19, 1477 (1983).
[4]R. C. Powell, Lin Xi, Xu Gang, Gregory J. Quarles, and J. C. Walling, Phys. Rev. B 32, 2788 (1985).
[5]M. L. Shand, J. C. Walling, and R. C. Morris, J. Appl. Phys. 52, 953 (1981).
[6]M. L. Shand and J. C. Walling, IEEE J. Quantum Electron. QE-18, 1152 (1982).
[7]M. L. Shand and H. P. Jenssen, IEEE J. Quantum Electron. QE-19, 480 (1983).
[8]R. Englman, B. Champagnon, G. Duval, and A. Monteil, J. Lumin. 28, 337 (1983).
[9]S. K. Gayen, W. B. Wang, V. Petričević, R. Dorsinville, and R. R. Alfano, Appl. Phys. Lett. 47, 455 (1985).
[10]S. K. Gayen, W. B. Wang, V. Petričević, and R. R. Alfano, Proceedings of the International Conference on Lasers '85, 2–6 Dec. 1985, Las Vegas, Nevada.
[11]M. J. Romanelli in *Mathematical Methods for Digital Computers*, edited by A. Ralston and H. S. Wilf (Wiley, New York, 1960), p. 110.
[12]A. Yariv, *Quantum Electronics*, 2nd ed. (Wiley, New York, 1975), p. 163.
[13]R. Englman, *Non-radiative Decay of Ions and Molecules in Solids* (North-Holland, Amsterdam, 1979), p. 50.

RAPID COMMUNICATIONS

This section was established to reduce the lead time for the publication of Letters containing new, significant material in rapidly advancing areas of optics judged compelling in their timeliness. The author of such a Letter should have his manuscript reviewed by an OSA Fellow who has similar technical interests and is not a member of the author's institution. The Letter should then be submitted to the Editor, accompanied by a LETTER OF ENDORSEMENT FROM THE OSA FELLOW (who in effect has served as the referee and whose sponsorship will be indicated in the published Letter), A COMMITMENT FROM THE AUTHOR'S INSTITUTION TO PAY THE PUBLICATION CHARGES, and the signed copyright TRANSFER AGREEMENT. The Letter will then be published without further refereeing. The latest Directory of OSA Members and Fellows, is published in the August 1985 issue of Optics News.

Optical computing using hybrid encoded shadow casting

Yao Li, George Eichmann, and R. R. Alfano

University of New York, City College, New York, New York 10031.

Received 19 May 1986.
Sponsored by H. John Caulfield, University of Alabama in Huntsville.
0003-6935/86/162936-03$02.00/0.

The parallel processing property of optics has been recognized as the main driving force behind digital optical computing.[1,2] A parallel pattern logic operation, first proposed by Tanida and Ichioka,[3,4] overlaps spatially coded 2-D binary pixel patterns situated in an optical input plane. These patterns, when illuminated by divergent light beams emanating from a group of LEDs, form different interlaced projections (shadows) representing different parallel logic operations in the optical output plane. Since the pattern overlap corresponds to a spatial domain filtering process, it is also known as optical shadow casting (OSC). Using OSC, a large number of 2-D binary[3,4] or multiple-valued[5,6] logic inputs can be parallel processed. Another pattern logic method, proposed by Bartelt *et al.*,[7] uses theta modulation to encode the signal grey-level values into different grating orientations. The combination of these grey-level-dependent gratings form the logic inputs that are to be manipulated by a coherent optical processor. Using spatial-frequency domain filtering, different optical logic functions can be generated. Recently, Yatagai[8] described another pattern logic method in which the spatially encoded patterns are overlapped with an operational mask. Instead of using the OSC LED patterns, this method switches an operational mask for the different logic operations. However, in all these pattern logic methods, either the spatial filtering or pixel casting process is performed by either a transparent or opaque screen. In this communication, the use of a polarization encoding and filtering method to perform lensless OSC logic operations is proposed. Both linear orthogonally polarized and hybrid form polarizations with transparent/opaque mask input, logic signals are used. Using this polarization or hybrid encoded OSC (POSC), double- or triple-instruction logic operations can be performed. This technique can be extended to generate multivariable binary as well as two-variable multiple-valued logic functions and can also be used in conjunction with the Yatagai's pattern logic method. Pertinent examples such as the design of a binary full- and a ternary half-adder are presented.

In the proposed POSC, while the geometry is identical to the conventional lensless OSC, the logic inputs and outputs are represented by the sense of polarization. Take the two-variable (A and B) binary logic as an example (see Table I). These variables are represented by the two polarization encoded masks (the second and third columns of Table I), where the symbols—and| denote the two linear, parallel and perpendicular, polarizations representing the physical x and y directions, respectively. The two thus encoded input masks (see the fourth column of Table I where ∧ denotes the overlap) are illuminated by a group of four nonpolarized LED sources. When three of the four LEDs (see the first column of Table I) are on, corresponding to four overlapped input patterns, on the output screen four different projections are formed. In each of the four cases, two cross-polarized light patterns can simultaneously exist. The $x(y)$-polarized output plane center cell pattern corresponds to the logic operations A NAND B (A OR B), respectively. Thus a fixed LED source pattern and the rotation of the output center-cell polarizer allow the implementation of two different binary logic functions. By removing the output polarizer, a third binary function, the superposition of the two cross-polarized patterns, can also be generated. With a OSC, because the opaque part of the screen blocks the light, the mutually transparent part of the overlapped inputs is limited to be only a quarter of the mask area. With a POSC, the mutually transparent input mask area is doubled (with each half transparent to one of the two orthogonal linear polarizations). Therefore, for a fixed source and input pattern, two orthogonal transmission channels exist.

Orthogonally polarizing LEDs can also be used as light sources. In this case, the overlapped transparent masks respond only to $x(y)$-polarized LEDs. Using different combinations of polarized LEDs, different binary logic functions can be implemented. In Table II(a), using either unpolarized on/off or orthogonally polarized input LED states, the generations of all sixteen two-variable binary logic functions

Table I. Example of POSC Input Output Signal as well as LED Source Encodings. The symbols — and | Represent x and y Polarizations, and ∧ denotes the Input Overlap.

LED source	INPUT A	INPUT B	INPUT A∧B	OUTPUT pattern	OUTPUT function
○ ○	— 0	— 0	—		
○ ●	— 0	|	—		$f_- = \overline{A \cdot B}$
	|	— 0	—		$f_1 = A+B$
	|	|	|		$f_{-1} = 1$

Table II. Sixteen Possible POSC Two-Variable, with Inputs Encoded with Either Variables *A* and *B* (a) or variables *A* and *C* (b), Logic Operations. Both Transparent/Opaque and Orthogonal Polarization Input LED States are Used.

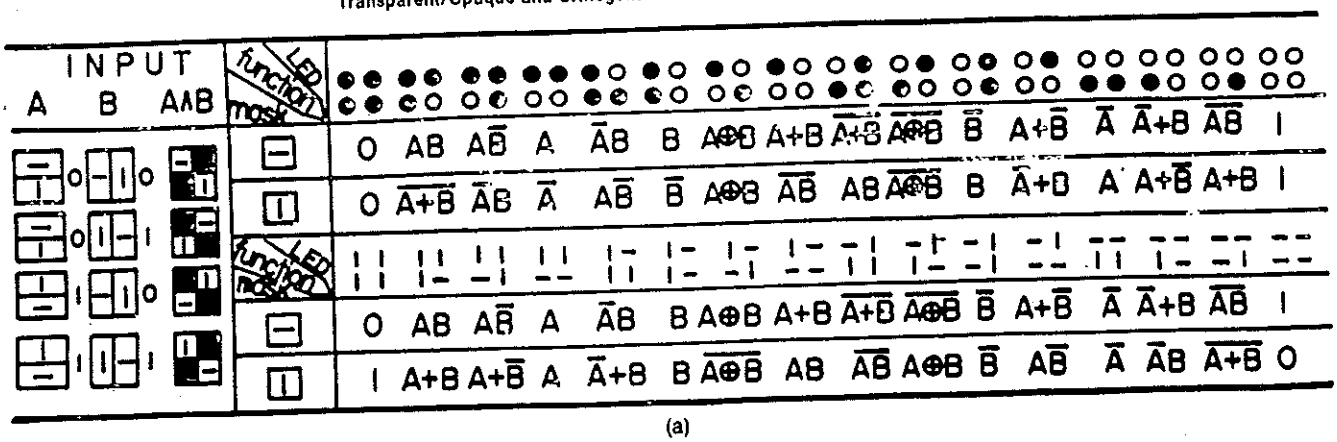

(a)

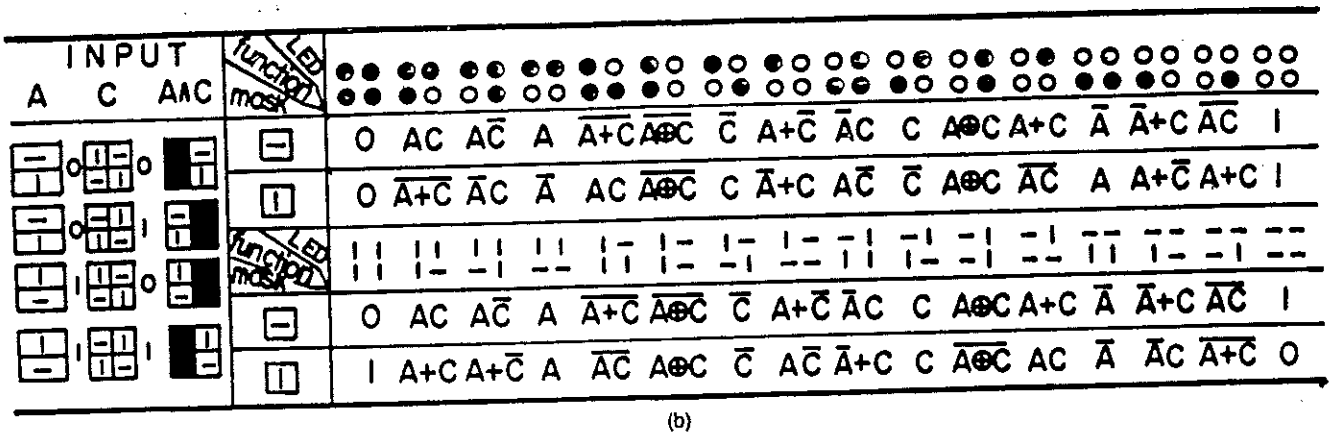

(b)

are summarized. For unpolarized LEDs, either output state can be obtained from the other by interchanging (for both variables) the zero and the one logic assignments. For polarized LEDs, the cross-polarized outputs represent positive- and negative-true logic functions, respectively. In addition to the input codes shown in Table I, other input encoding methods where the overlapped input patterns preserve, for the two orthogonal polarizations, the two mutually transparent parts, are also possible. In Table II(b), for the variable *C*, an alternative input variable encoding is shown. For the variables *A* and *C*, the corresponding sixteen logic function generations are also shown. It has been indicated that a conventional single-element OSC processor is a single-instruction multiple-data (SIMD) machine. Using POSC, both double- and triple-instruction logic processing can be performed. If in the previous example we locate three different detectors at the center cell of the output screen, with the first (second) being $x(y)$ polarized, and the third unpolarized, three different functions can be simultaneously processed. Therefore, a single-element POSC represents a multiple-instruction multiple-data (MIMD) machine.

In binary optical computing, implementation of multivariable logic functions are needed. For example, for binary addition, to generate both the output sum and the carry, three variables need to be used. To perform binary OSC addition to preserve symmetry, Kozaitis and Arrathoon[5] have used four rather than three variables. One of the four

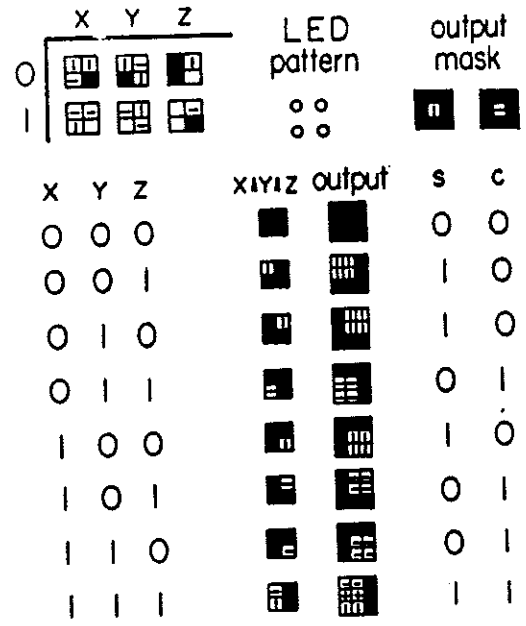

Fig. 1. Single-element POSC binary full-adder. A hybrid input polarized patterns correspond to the sum and carry outputs, respectively.

variables, however, is kept at zero during the operation. With this method, the detectable output signal area is reduced to a quarter of the previously used two-variable area. This size reduction limits, due to diffraction effect, the pixel integration area. To achieve a reasonable output, larger input pixels must be used. The use of POSC leads to larger aperture (identical to two-variable case) three-variable binary logic operations. Using three differently encoded variables A, B, and C [see Tables II(a) and (b)], the overlap among three inputs will always contain a mutually transparent area to either one of the two orthogonal linearly polarized beams. The use of the eight possible input overlaps, together with a group of LEDs, can generate two[8] three-variable binary logic functions. For a one-bit binary full-adder, two parallel POSC elements, one for the sum and the other for the carry, need to be used. Because the POSC is a MIMD machine, using other input encoding schemes, it is possible to perform a single-POSC-element binary addition. For example, in Fig. 1 a single-element POSC binary full-adder is shown. Here the input uses hybrid (both transparent/opaque and orthogonal polarization) codes. In the first four columns of Fig. 1, the input variables X, Y, and Z and their corresponding overlaps are shown. When all four unpolarized LEDs are on, the two cross-polarized patterns in the center cell of the output plane represent the resultant sum and carry bits, respectively. Thus, using two, one x and the other y polarized, detectors at the output center cell, a single-element POSC binary full adder can be constructed.

The similar idea can be applied to two-variable tenary logic computing. For each input variable, three mutually orthogonal states representing the symbols 0.1, and 2, respectively, are required. For the nine possible overlaps among the two ternary input variables, a mutually transparent area must be provided. The use of the two orthogonal polarizations in the four corners of the overlapped pattern produces eight different states. The ninth state is encoded as an unpolarized but transparent corner. As an example, consider the operation of a two-variable POSC ternary half-adder. In Fig. 2, the hybrid form of input variables A and B are shown. Using the input variable truth table (the first two columns) in the third column the nine possible two variable A and B overlap forms are shown. One of the overlap patterns is forced to be opaque. The sum output symbols, 0, 1, and 2, are encoded as opaque y- and x-polarized signals, respectively. Correspondingly, in the fourth column, the LED source and the center cell output patterns are shown. The results, shown in the fifth column, are obtained from the two x- and y-polarized center cell detectors. To generate the carry another POSC cell must be employed. For this carry, in the sixth and seventh columns, the corresponding LED pattern and the output unpolarized detection results are shown.

To summarize, an efficient polarization encoding and filtering method to perform OSC optical computing is proposed. Inputs are spatially encoded with either polarized or both polarized and transparent/opaque pixels. Either polarized or unpolarized LED input source arrays can be used. At the center cell of each output element, depending on different parallel polarization filters, three different logic functions can be obtained. In addition to the two-variable binary. The POSC method is suitable for large aperture multivariable binary and the two-variable ternary optical computing. Using liquid crystal e-o material sandwiched between $\lambda/2$ plates and linear polarizers, real-time polarization encoding can be performed leading to optical parallel processing of a large amount of data.

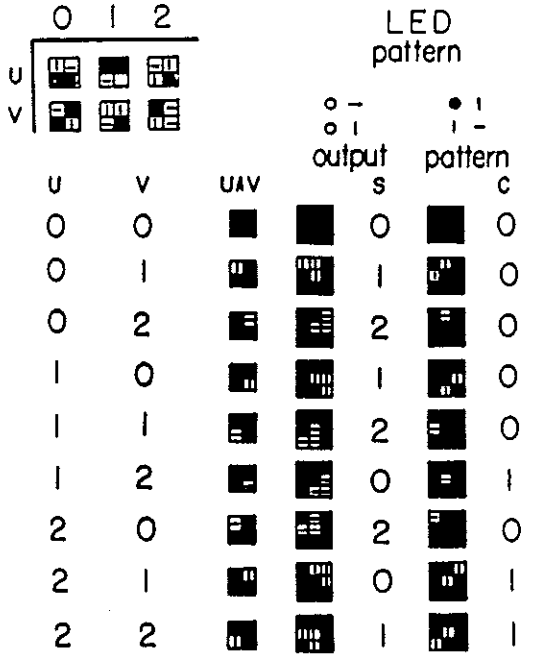

Fig. 2. POSC ternary half-adder. The hybrid input code is used. The output sum symbols 0.1 and 2, are encoded as opaque y and x-polarized signals, respectively. For the carry, both polarizations are used.

This work is supported in part by a grant from the Air Force Office of Scientific Research.

References

1. C. C. Guest and T. K. Gaylord, "Truth-Table Look-up Optical Processing Utilizing Binary and Residue Arithmetic," Appl. Opt. 19, 1201 (1980).
2. A. A. Sawchuk and T. C. Strand, "Digital Optical Computing," Proc. IEEE 72, 758 (1984).
3. J. Tanida and Y. Ichioka, "Optical Logic Array Processor Using Shadowgrams," J. Opt. Soc. Am. 73, 800 (1983).
4. Y. Ichioka and J. Tanida, "Optical Parallel Logic Gates Using a Shadow-casting System for Optical Digital Computing," Proc. IEEE 72, 787 (1984).
5. S. Kozatis and R. Arrathoon, "Shadow Casting for Direct Look-up and Multiple-Valued Logic," Appl. Opt. 24, 331
6. R. Arrathoon and S. Kozatis, "Shadow Casting for Valued Associative Logic," Opt. Eng. 25, 29 (1986).
7. H. Bartelt, A. W. Lohmann, and E. E. Sicre, " Processing in Parallel with Theta Modulation," A 1, 944 (1984).
8. T. Yatagai, "Optical Space-Variant Logic-G Spatial Encoding Technique," Opt. Lett. 1